Original

Nowak, G.; Stoermer, M.; Becker, H.-W.; Horstmann, C.; Kampmann, R.;
Hoeche, D.; Haese-Seiller, M.; Moulin, J.-F.; Pomm, M.; Randau, C.;
Lorenz, U.; Hall-Wilton, R.; Mueller, M.; Schreyer, A.:

Boron carbide coatings for neutron detection probed by x-rays, ions, and neutrons to determine thin film quality

In: Journal of Applied Physics (2015) AIP

DOI: 10.1063/1.4905716

Boron carbide coatings for neutron detection probed by x-rays, ions, and neutrons to determine thin film quality

G. Nowak,[1,a)] M. Störmer,[1] H.-W. Becker,[2] C. Horstmann,[1] R. Kampmann,[1] D. Höche,[1] M. Haese-Seiller,[3] J.-F. Moulin,[3] M. Pomm,[3] C. Randau,[4] U. Lorenz,[1] R. Hall-Wilton,[5] M. Müller,[1] and A. Schreyer[1]

[1]*Helmholtz-Zentrum Geesthacht, Max-Planck-Straße 1, 21502 Geesthacht, Germany*
[2]*RUBION-Zentrale Einrichtung für Ionenstrahlen und Radionuklide, Ruhr-Universität Bochum, 44780 Bochum, Germany*
[3]*Helmholtz-Zentrum Geesthacht, Außenstelle an der Forschungsneutronenquelle Heinz Maier-Leibnitz (FRM II), Technische Universität München, 85747 Garching, Germany*
[4]*Georg-August Universität Göttingen, Geowissenschaftliches Zentrum, 37077 Göttingen, Germany and Außenstelle an der Forschungsneutronenquelle Heinz Maier-Leibnitz (FRM II), Technische Universität München, 85747 Garching, Germany*
[5]*European Spallation Source ESS AB, P.O. Box 176, 221 00 Lund, Sweden*

(Received 25 July 2014; accepted 17 December 2014; published online 16 January 2015)

Due to the present shortage of ^{3}He and the associated tremendous increase of its price, the supply of large neutron detection systems with ^{3}He becomes unaffordable. Alternative neutron detection concepts, therefore, have been invented based on solid ^{10}B converters. These concepts require development in thin film deposition technique regarding high adhesion, thickness uniformity and chemical purity of the converter coating on large area substrates. We report on the sputter deposition of highly uniform large-area $^{10}B_4C$ coatings of up to 2 μm thickness with a thickness deviation below 4% using the Helmholtz-Zentrum Geesthacht large area sputtering system. The $^{10}B_4C$ coatings are x-ray amorphous and highly adhesive to the substrate. Material analysis by means of X-ray-Photoelectron Spectroscopy, Secondary-Ion-Mass-Spectrometry, and Rutherford-Back-Scattering (RBS) revealed low impurities concentration in the coatings. The isotope composition determined by Secondary-Ion-Mass-Spectrometry, RBS, and inelastic nuclear reaction analysis of the converter coatings evidences almost identical ^{10}B isotope contents in the sputter target and in the deposited coating. Neutron conversion and detection test measurements with variable irradiation geometry of the converter coating demonstrate an average relative quantum efficiency ranging from 65% to 90% for cold neutrons as compared to a black ^{3}He-monitor. Thus, these converter coatings contribute to the development of ^{3}He-free prototype detectors based on neutron grazing incidence. Transferring the developed coating process to an industrial scale sputtering system can make alternative ^{3}He-free converter elements available for large area neutron detection systems. [http://dx.doi.org/10.1063/1.4905716]

I. INTRODUCTION: MOTIVATION

The detection of a neutron radiation field has a broad spectrum of applications from life sciences,[1] material investigation, and engineering[2] to neutron monitoring in nuclear power plants and nuclear material survey as, for example, in the U.S. homeland security program.[3] In large-scale neutron research facilities, neutron scattering is used to decipher inter-atomic and inter-molecular structure in the range of spatial distances from sub Å to hundreds of nanometers under externally given conditions.[4] For this purpose, neutron scattering experiments[5,6] are performed with so-called thermal and cold neutrons of wavelengths of the order of the typical inter-atomic ($\sim$1 Å) and inter-molecular ($<$10 Å) distances. Successful planning and long-term operation of a large-scale neutron scattering facility requires a robust detection concept with high neutron efficiency for thermal and cold neutrons. Since the price of detector scales with its size, cost-saving solutions are desired to replace ^{3}He-based detectors as they are used until today.

Neutrons, as particles without net electric charge, can only be detected via nuclear conversion reactions: these reactions generate charged particles, which can be detected by subsequent interaction processes like ionization of gas due to their charge. The conversion rate of neutrons and nuclei in a nuclear reaction into reaction products depends strongly on the nuclear-related neutron capture cross-section and the neutron energy. Given a particular energy range of neutrons, the choice of the converter material and the converter geometry is essential for a high conversion rate: It strongly determines the quantum efficiency of a neutron detector. The converter material is chosen so as to find a compromise between conversion efficiency, affordability, and workability.

The most common isotopes used for neutron detection are ^{3}He, ^{6}Li, ^{10}B, ^{155}Gd, and ^{157}Gd. Unfortunately, the isotopes ^{155}Gd and ^{157}Gd are extremely rare and difficult to obtain by centrifugation. The high capture cross section for thermal neutrons[7,8] and the chemically inert character of ^{3}He make it very suitable for detection applications. However,

a)Author to whom correspondence should be addressed. Electronic mail: Gregor.Nowak@hzg.de. Tel.: +49 4152 87 2560.

since the generation of ^{3}He as a byproduct of nuclear weapons storage is ceasing, its availability is nowadays very limited and consequently ^{3}He is becoming increasingly expensive;[9,10] the price raises continuously (nowadays: >2500 $/(bar liter)). Furthermore, research activities in other fields like on fusion reactors for energy generation by aneutronic nuclear fusion will need in the near future substantial amount of ^{3}He for the $D + {}^3He \rightarrow p(14.7\,\mathrm{MeV}) + \alpha(3.6\,\mathrm{MeV}) -$ reaction.[11,12] ^{6}Li as a converter material demands a chemical protective coating because of its chemical reactivity with water vapor when handled at ambient conditions or a detector assembly unit filled with inert gas. ^{6}LiF as a converter coating is itself stable at ambient conditions but as a salt it is electrically an insulator. Therefore, ^{6}LiF converter coatings in neutron detectors need an additional conductive coating for draining the charges produced by nuclear conversion reaction in detection applications. The natural abundance of ^{10}B is about 6×10^8 times higher than that of ^{3}He,[9,13–15] and the isotope is readily obtained by centrifugation. However, the gaseous compound $^{10}BF_3$ is to be avoided due to its toxicity.

In this situation, alternative materials for neutron detection are highly welcomed since the quantitative need for neutron converters increases as new large-scale neutron research facilities are planned.[3,4] A promising candidate material is the solid compound $^{10}B_4C$, which is efficiently converting, affordable, and workable. The $^{10}B_4C$ compound is enriched up to 95 at. % with the ^{10}B isotope (in the boron component) compared to natural B_4C, which contains about 20 at. % of ^{10}B and 80 at. % of ^{11}B in the boron component. $^{10}B_4C$ solid state neutron converter detectors are highly interesting for large area neutron detection and for replacing gas detectors using expensive ^{3}He or toxic BF_3. However, the alternative and safe ^{10}B solid state neutron converter detector technology is still in the early stages of development.[15–18]

A. Neutron detection by ^{10}B

The neutron capture nuclear reaction for ^{10}B has two branches

$$^{10}\mathrm{B} + {}^1_0n \rightarrow {}^7\mathrm{Li}\,(\mathrm{at}\,0.840\,\mathrm{MeV}) + \alpha(\mathrm{at}\,1.470\,\mathrm{MeV}) + \gamma(0.482\,\mathrm{MeV}) \quad (\mathrm{A}) \quad (94\%)$$
$$\rightarrow {}^7\mathrm{Li}\,(\mathrm{at}\,1.015\,\mathrm{MeV}) + \alpha(\mathrm{at}\,1.777\,\mathrm{MeV})\ (\mathrm{B})\ (6\%).$$

For thermal and cold neutrons, the neutron capture cross section as a function of the kinetic neutron energy E goes with $\sim\sqrt{E}$.[19,20] The probability for neutron capture is directly connected to the neutron speed, i.e., to the period of time in which the neutron is close enough to a nucleus to be captured. ^{10}B has a capture cross section of about of 3800 barn for thermal neutrons, which corresponds to 72% of the thermal neutron capture cross section of ^{3}He. Taking into account the number density of ^{10}B atoms in solid state, the resulting mean free path for thermal neutrons in ^{10}B is about 20 μm.[21] Proportional gas detectors and $^{10}B_4C$ solid state converter detectors have a very similar detection concept,[15] so that the gas detector technology could largely be transferred to the boron detector. A solid state neutron detector is a proportional detector containing a solid state ^{10}B-rich neutron converter layer in direct contact to the detection gas ($Ar(80\%)/CO_2(20\%)$). The converter is required because neutrons do not ionize the detection gas directly. Neutron capture by ^{10}B atoms in the converter layer produces ^{7}Li and He ions with high kinetic energy. The ion range of these ^{7}Li and α in the converter material is determined by the kinetic energy resulting from the nuclear reaction and by the stopping power inside the converter layer.[22,23] For a successful detection process, one of these ions is required to escape out of the converter layer and ionize the detection gas in the proximity of the converter, producing there free electrons which become accelerated towards the anode wire which is at high voltage. These accelerated electrons collide with gas molecules and ionize them and produce in this way charge avalanches. The latter generates pulses on the anodes and cathodes of the detector, which are amplified, discriminated, and then interpreted as neutron events by the read-out and data acquisition system.

In this report, the relative quantum efficiency is chosen as the figure of merit of the converter coatings, and is defined as the ratio of neutrons detected by the solid state converter (in a certain energy band) and by a conventional ^{3}He monitor (with a diameter of 1 in. filled with 10 bars) under identical conditions.

Two intrinsic properties of the converter material—the absorption for neutrons and the stopping power for the conversion reaction products—define the optimum converter medium thickness d_{B4Copt} and the optimum incident angle Θ_{in} for the best figure of merit of the converter coating. After the conversion reaction, the products, ^{7}Li and α, leave the point of conversion in isotropic trajectories, but in opposite directions for thermal neutron interactions. The kinetic energies of the escaping ions are determined by the conservation of momentum and energy during the nuclear reaction[24,25] and the stopping power of these ions in solid ^{10}B. For the conversion reactions (A) and (B), the maximum ranges $d_{max\ range}$ of α and ^{7}Li ions in ^{10}B are[15,24,25]

(A) : Ion range for α-particle: 3.2 μm and for ^{7}Li ion: 1.5 μm (94%).
(B) : Ion range for α-particle: 3.9 μm and for ^{7}Li ion: 1.7 μm (6%).

Thin neutron absorber layers are required in order to obtain high reaction product escape probability and, consequently, high neutron efficiency. Simultaneously, a sufficiently large absorption length in the converter medium needs to be provided for the incident neutrons to ensure an effective absorption process. Both requirements are met for shallow incidence angles of the neutron beam on the thin converter layer. In this particular geometry, in which the converter surface is inclined with respect to the incident beam, the path for absorption is prolonged for a thin converter film, while the length of the escape path in direction perpendicular to the convert surface remains short.

The detection concepts based on thin film converters require a uniform coating of the converter material over a large area. In this paper, we present a suitable coating process for producing highly adhesive, uniform, and chemical

pure ^{10}B layers. The quality of these coatings is evaluated in terms of the performance and neutron detection efficiency. For example, a long term adhesion stability of the coatings on the substrate is absolutely obligatory. A uniform signal response over the entire active area is fundamental to a functional 2D detector, thus a uniformity of the coating thickness within a range of few percent is required. Moreover, the intrinsic thermal neutron detection efficiency must be comparable to that of a ^3He detector, if the solid state neutron conversion detector is to be an alternative worth considering. Furthermore, the content of impurities such as hydrogen in the converter coatings and substrates should be as low as possible to avoid diffuse scattering of neutrons. Finally, the fabrication costs for the B_4C converter coatings have to be competitive, and the implementation of these $^{10}B_4C$ converter coatings in detector technology should result in no financial disadvantage, or even a benefit, as compared to the costs of a ^3He based detector.

Motivated by these considerations outlined above, the Helmholtz-Zentrum Geesthacht (HZG) developed $^{10}B_4C$-conversion layer neutron detectors in inclined geometry in cooperation with the industrial partner DENEX GmbH (Lüneburg, Germany) as an in-kind contribution to the development of components for the European Spallation Source (ESS). The converter coatings discussed here can be implemented in a number of conceptually different detector designs.[26–29]

B. General properties and application of boron carbide

While being a well-suited material for neutron detection via conversion reactions, B_4C is mainly known for its broad spectrum for technical applications as a hard material. B_4C possesses an outstanding hardness (25–30 GPa) at a low density (2.52 g/cm^3) combined with a high thermal stability (melting point: 2760 °C).[30,31] A comprehensive review concerning the wide homogeneity range (8.8–20 at. % carbon) in the compound of boron carbide and its comprehensive phase diagram are presented in Ref. 32. A large variety of preparation methods for boron carbide powder and bulk samples yield a wide range of variation of mechanical properties such as hardness or density.[32]

B_4C coatings in the homogeneity range mentioned above solidify in a rhombohedral structure at short range for substrate temperatures below 900 °C during deposition. For substrate temperature above 950 °C, a variety of crystalline phases occur.[33,34] X-Ray Diffraction (XRD)-studies on crystalline B_4C show the unit cell consisting of a rhombohedron with B_{12} icosahedra at each corner.[32,35] The space group of B_4C is $R\bar{3}m$(166).[32,35] There are two types of spatial arrangements of the B_{12} icosahedral clusters called α- and β-type structure.[36] B_4C possesses electronic properties of a semiconductor.[32] In a first attempt, RF-sputtering modes were used to fabricate B_4C coatings for optical applications.[33,37,38] DC-sputtering modes were also investigated for coatings of cutting tools[39] as well as for $^{10}B_4C$ coatings on large areas.[18] The reported B_4C layer thicknesses range from several nm up to several μm. Typically, sputtered boron carbide films with thicknesses above a few hundred nm tend to delaminate from the substrate because of compressive stress induces by the sputtering process.[39,40] Fabrication of boron carbide coatings by evaporation methods was demonstrated and film thicknesses up to 20 μm were reported, but the deposited areas were of comparatively small size (several cm^2).[41–44]

The present report describes the preparation of B_4C coatings by DC magnetron sputtering on Si and Al substrates. Further, it discusses the results of thorough structural characterization (by spectral reflectance and profilometry, XRD, Scanning Electron Microscopy (SEM), and X-Ray Reflectometry (XRR)) as well as chemical and isotopic analysis (by X-ray-Photoelectron Spectroscopy (XPS), Secondary-Ion-Mass-Spectrometry (SIMS), and nuclear reaction analysis (NRA)). Neutron quantum efficiency of $^{10}B_4C$ coatings was measured at the TOF reflectometer beam line REFSANS at MLZ. The perspective of this discussion is focused on the performance of the B_4C coatings for 2-D neutron detection applications. The magnetron sputtered boron carbide coatings exhibit outstanding structural and compositional quality and show high potential in application as neutron converter for the detection of cold and thermal neutrons.

II. EXPERIMENTAL: SAMPLE PREPARATION AND CHARACTERIZATION

The $^{nat.}B_4C$ and $^{10}B_4C$ coatings are produced in the HZG-sputtering facility. The sputtering system has a base pressure in the range of 10^{-8} mbar and is designed for high-precision depositions of single layers and multilayers X-ray mirrors.[45,46] The sputtering facility is equipped with a sample holder of 1500 mm length. During deposition, this sample holder is translated in front of the sputter targets at a velocity $v_{sputter}$, which determines the deposition rate and therefore the thickness. A programmed sequence of velocities results in a thickness profile on the substrate. For deposition of the $^{nat.}B_4C$ and $^{10}B_4C$ coatings, two planar targets of 300 mm × 90 mm in size were fixed on a water-cooled copper backing plate. Using two sputtering sources doubles the sputter yield and therefore increases the throughput of coatings. The targets were purchased from RHP Technology. The enrichment of the primary $^{10}B_4C$ powder on ^{10}B for the sintering process of $^{10}B_4C$ targets is about 95% as reported by the supplier RHP technology. For the sputtering process, Ar with a purity of 99.99999% (Argon 7.0) was used as working gas for the sputtering process. The Si substrates (20 mm × 60 mm) were cleaned with acetone and wiped dry by lint-free tissue and finally blown by dust-free, compressed air. The rolled Al plates (100 mm × 100 mm × 0.5 mm, 99.5% Al) were mechanically treated[47] and chemically cleaned with ordinary liquid hand washing tenside and water to remove grease and oils from the rolling process. Finally, the Al plates were blown dry by dust-free compressed air. The long edge of the Si substrates can be mounted either parallel or perpendicular to the direction of motion of the sample holder during the deposition. Up to 13 Al plates can be mounted in one row on the sample holder. Every Al plate is fixed by two holders (width 10 mm on opposite sides of the Al plate (see Fig. 1). An additional Si substrate coated with Ti prior to B_4C deposition is mounted at the end of the Al

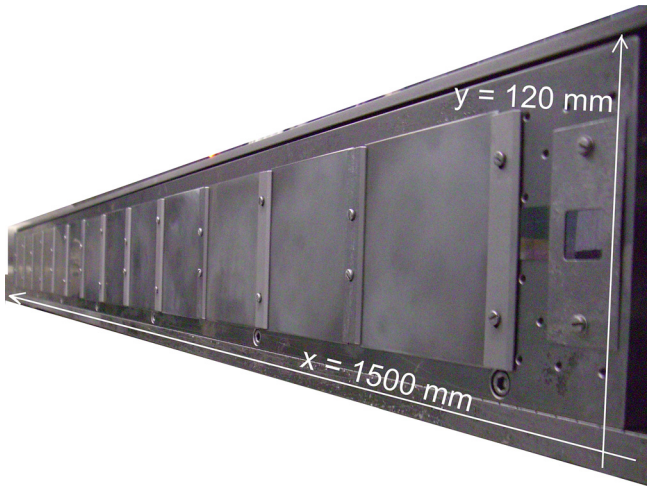

FIG. 1. Front view of the sample holder with 13 coated Al-plates, each 100 mm × 100 mm, and one Si substrate at the right edge. During deposition, the whole assembly is moved in x-direction. Reproduced by permission from European Spallation Source—Technical Design Report, ESS-2013-001, 2013. Copyright 2013 European Spallation Source.

plate row and partially covered with a mask, to produce a coating step during the deposition. The coating step height is used to check the boron carbide coating thickness for the current deposition run by profilometry measurements.

The thickness determination of the boron carbide coatings is performed by two methods, depending on the coating thickness.

For coatings of less than 100 nm thickness, XRR is employed using the Bruker D8 system in Bragg-Brentano geometry with Mo-K_α radiation. The measured reflectivity curves were simulated with the commercial program Bruker/REFSIM.[48]

For coatings thicker than 100 nm (i.e., beyond the resolution limit and penetration depth of the XRR setup), the film thickness and thickness uniformity were measured with a Dektak M6 stylus profilometer on the coating edge on the control sample (Si/Ti substrate). The step height difference from the substrate level to the surface of the B_4C coating corresponds to the B_4C layer thickness. The characterization of the coating thickness uniformity was performed by a series of film step height measurements for test samples.

Thickness uniformity of the entire 100 mm × 100 mm Al converter plates was verified by spectral reflectance, based on the interference and reflection of a broad light spectrum at a thin, optically transparent layer. The Fast Fourier Transformation of the interference pattern of the reflected light spectra allows tracing back the reflecting layer thickness if the optical density of the layer is known. This non-destructive method is well-suited for thickness monitoring especially on large areas.[49] An equidistant grid of 81 points was used here to scan the 100 mm × 100 mm sample area. The F20-EXR/NIR optical system was provided by the Filmetrics GmbH, Germany.

The presence of crystallinity in the coatings was investigated by XRD and cross checked by means of SEM.

The chemical composition throughout the depth of the coating was profiled by XPS and by SIMS. Alternating local etching with XPS and SIMS allows extending these intrinsically surface limited methods into the sample depth. As SIMS is sensitive to the ion mass, also depth resolution of the ratio of ^{11}B to ^{10}B isotopes in the coating is achieved. Etching was performed using a Mini Beam sputter gun operating at 4 kV using Ar process gas. The XPS setup (Kratos Axis Ultra DLD) is equipped with a 15 kV X-ray gun, which emits monochromatic Al-K_α-radiation and the Bremsstrahlung continuum. The chemical composition analysis of films manufactured by the sputter deposition process is motivated by the element specific sputter yield. In case of targets consisting of two or more elements, the stoichiometry of the deposited film can differ from that of the target in the steady state of material erosion.[50] Therefore, films resulting from relatively long lasting sputter deposition processes need to be checked for their chemical composition. The analysed area size for XPS was 700 × 300 μm^2 and the pass energy was set to 20 eV during region scans (energy resolution of 0.1 eV).

The SIMS setup consists of a Hiden analytical system with a MAXIM Quadrupole mass spectrometer with a mass resolution of $\Delta m < 0.1$ a.u. The relative heights of SIMS signals for the isotopes of one element are proportional to their relative amounts. For analysis, the signal was taken out of an inner gate of about 150 μm × 100 μm from the rastered and etched area of 650 × 450 μm^2. A focused ion beam with a diameter of 100 μm was provided to the SIMS set-up by an IG20 ion gun operating at 5 kV and a beam current of about 500 nA.

These locally destructive methods were complemented by the non-destructive ion beam analysis method of Rutherford-Back-Scattering (RBS), and NRA of the $^{10}B(\alpha,p)^{13}C$ reaction, which is only sensitive to ^{10}B. In these methods, any parasitical chemical contaminations of the investigated film are excluded since no etching procedure is required. The resonant nuclear reaction $H(^{15}N,\alpha\gamma)^{12}C$ was employed to determine the level of hydrogen impurity in the converter coating. Hydrogen as a dissociation product of water is a frequent gas component in vacuum systems and can be incorporated into the film during deposition. For both RBS and the $^{10}B(\alpha,p)^{13}C$ nuclear reaction analysis, an accelerated beam of α particles (2 MeV) hits the converter film. An α-particle-sensitive silicon detector was positioned at an angle of 160° with respect to the incident ion beam. The RBS spectra were analysed by RBX computer code.[51] For the analysis, a stratified mass model for the sample is assumed. The distribution of masses in the layer depth and the thicknesses of these layers are free parameters for the fitting routine. The resulting layer model can be interpreted as an isotopic and chemical depth profile of the sample.

For the nuclear reaction analysis of the ^{10}B isotope content in the boron carbide coatings, the protons become detected resulting from the reaction $^{10}B(\alpha,p)^{13}C$ on the ^{10}B-isotope induced by the α-particles. The integral intensity of the proton peaks can be directly converted into a ^{10}B concentration by comarison of proton intensity from a natural boron sample with a known composition. This method allows the determination of the relative frequentness of the ^{10}B isotope in an ensemble of boron atoms with the accuracy of typically less than 1 at. %.[52] The error depends also of cause on the precision of knowledge about the concentration in the sample for comparison.

For the depth profiling of the H-distribution in the coatings, the resonant nuclear reaction $H(^{15}N,\alpha\gamma)^{12}C$ was employed using the narrow resonance at the ^{15}N energy of 6.4 MeV.[53] The kinetic energy of the perpendicular incident ^{15}N beam on the sample was successively increased. By increasing the energy of the ^{15}N ions, the reaction occurs in larger depth of the sample. The number of γ-quants from the reaction is recorded in a 4π NaI-detector. This intensity in dependence of the beam energy can be converted to a hydrogen concentration in dependence of depth. The nuclear analysis measurements were carried out at Zentrale Einrichtung für Ionenstrahlen und Radionuklide (RUBION), Ruhr-Universität Bochum, Germany.

The relative quantum efficiency of the converter coatings was characterized at the REFSANS ToF-beam line (Meier-Leibniz Zentrum, Garching), making use of a test detector developed by a cooperation of HZG and the DENEX GmbH. This test detector with an active area 200 mm × 200 mm was used for measuring the quantum efficiency as a function of the neutron incident angle on the converter coatings. The test detector design is specialized for a fast exchange of converter plates to investigate the properties of converter coatings deposited at a variety of growth conditions. The geometry of the test detector windows allows for perpendicular and for inclined incidence of the neutron beam onto the converter surface. The read out electronics of the test detector is based on delay line technique and is typically used for a Time of Flight (ToF)-measurement mode. The ToF-neutron Reflectometer REFSANS is operating at the end of a neutron guide connected to a cold neutron source. The neutron energy can be selected from a range of 2 to 30 Å with an energy resolution ranging from 0.2% to 10%= $\frac{\Delta\lambda}{\lambda}$. The beam height of the collimated beam can be chosen between 0 and 12 mm. A heavy load goniometer (up to 200 kg) allows for the manipulation of the heavy and complexly shaped test detector.[54,55] The neutron quantum efficiency measurements were carried out for $^{nat.}B_4C$ and $^{10}B_4C$ converter coatings with thicknesses of about 1 μm, deposited on Al plates.[56]

The energy dependent neutron flux of the primary beam was monitored with a ^{3}He gas detector. These monitor measurements were used for calibration of the primary beam and normalization of the data from the test detector. The monitor has a diameter of 1 in. and a ^{3}He pressure of 10 bars. It absorbs 99.99% of the incident cold neutrons. Therefore, such a monitor is often called "black."

III. RESULTS AND DISCUSSION

A. Layer thickness of boron carbide coatings

The quantum efficiency of a $^{10}B_4C$ converter layer depends strongly on the converter layer thickness if this thickness is comparable to the ion escape ranges (less than 2 μm for ^{7}Li ions). Therefore, a high thickness uniformity of the converter coating is needed to ensure uniform quantum efficiency over the entire converter layer area. Natural boron carbide samples with coating step edges for assessing the achievable thickness uniformity were produced on Si substrates in several deposition runs. The substrates were fixed at different positions on the sample holder (see Fig. 1) and the coating step edges were oriented either along the x- or the y-direction. The coating step height, i.e., the coating thickness, was measured by *ex situ* profilometry. The samples had thicknesses of 0.52 μm, 1 μm, 1.59 μm, 1.22 μm, and 2.02 μm. A point by point plotting of the coating thicknesses in x and y direction (see Fig. 1) is presented in Fig. 2.

Notably, for all thicknesses, the width of the error bars is 3% ± 1% of the respective film thickness. Independent of the absolute thickness of the coatings, their thickness is remarkably uniform. The thickness deviation of coatings reported here is about a factor of five smaller than reported in Ref. 18.

This result was verified by a spectral reflectance measurement. Beyond the verification of the profilometry measurements, the apparatus for spectral reflectance allows for a rapid, contact-free determination of the film thickness over a large area of coating. Moreover, this method does not require a coating step edge. The thickness of a $^{nat.}B_4C$ coating on a

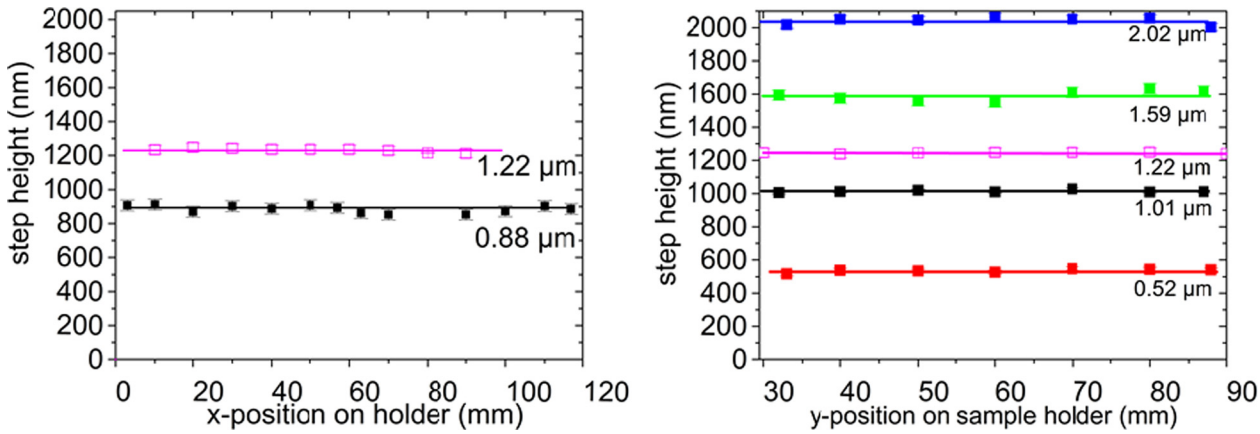

FIG. 2. Coating thickness uniformity in x (y = arbitrary) and y (x = arbitrary) direction on the sample holder as presented in Fig. 1. The error bars are in the order of 20–30 nm (see text). The open squares in magenta represent values extracted from the data shown in Fig. 3 (spectral reflectance) at y = 60 mm (left) and at x = 20 mm (right). Reproduced by permission from European Spallation Source—Technical Design Report, ESS-2013-001, 2013. Copyright 2013 European Spallation Source.

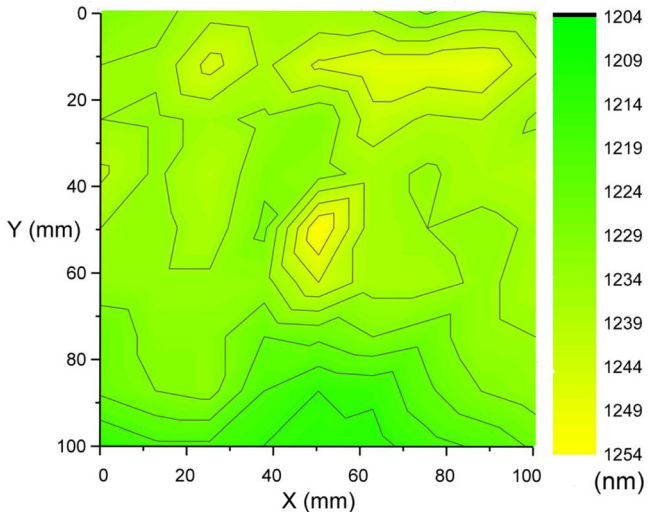

FIG. 3. 2-D thickness map (colour contour map) of a 100 mm × 100 mm area measured on a 1.22 μm thick boron carbide coating on Al by means of spectral reflectance (performed at the Filmetrics Company).

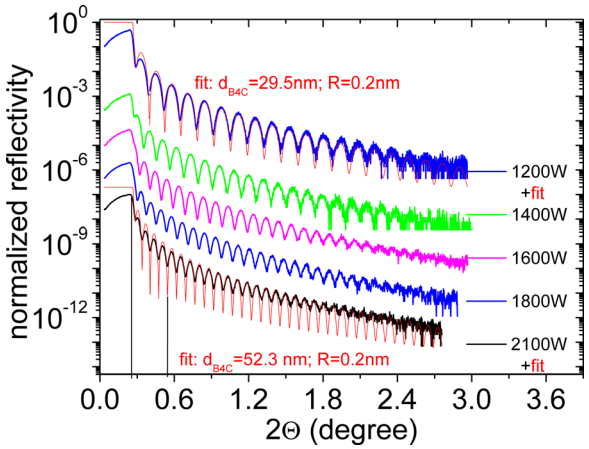

FIG. 4. Specular X-ray reflectivity measurements for a series of boron carbide films on Al_2O_3 substrates deposited at successively increased generator power. The radiation used is Mo-K$\alpha_{1,2}$. The intensities were shifted on the y-axis for a clearer illustration by multiplication factors.

100 mm × 100 mm Al plate was measured on a quadratic grid of 81 points with a spot size of 0.6 mm × 0.6 mm. The thickness distribution of the entire converter plate is presented in Fig. 3 as a colour contour map.

Statistical analysis of the spectral reflectance measurement yields a thickness uniformity of the 1.22 μm B_4C coating with a standard deviation of the thickness of ±2%. This result is in agreement with the 4% in peak to valley difference obtained from step height measurements with the stylus profiler. The scattering of data and the error bars are on the same level for both profilometry and spectral reflectance, demonstrating the comparability of the two methods. However, while the profilometry measurements took 3.5 h for the amount of data for Fig. 3, the spectral reflectance measurement was accomplished within 60 s.

A systematic increase of the power in the sputtering process from 800 W to 2100 W allows observing possible changes in the converter layer properties like mass density, layer thickness, surface roughness, adhesion to the substrate if sputtered at higher deposition rates. For each step in power, a 10 mm × 10 mm Al_2O_3 substrate was coated with a $^{10}B_4C$ thin film keeping the velocities $v_{sputter}$ of the sample holder constant. The choice of Al_2O_3 as substrate is only motivated by a larger X-ray contrast of the combination B_4C/Al_2O_3 compared to B_4C/Si.

The thicknesses of the coated films were measured by XRR specular X-ray reflectivity curves (see Fig. 4). In this series of reflectivity curves, the critical angle is at a constant position of $\theta = 0.14°$. This fact allows the conclusion that under the chosen sputtering conditions there is no variation in the density of the sputtered $^{10}B_4C$ coating as a function of the generator power.[57] The choice of sputtering parameters therefore does not modify the density of $^{10}B_4C$ layers coatings and it is expected that their efficiency in neutron conversion should be constant.

In addition, the frequency of the Kiessig fringes rises with increased applied power, indicating thicker $^{10}B_4C$ films at constant velocity $v_{sputter}$. By fitting the reflectivity curves with the simulation program REFSIM, the thickness, density, and roughness of each $^{10}B_4C$ film were determined. Since the holder velocity was constant at $v_{sputter} = 0.475$ mm/s for all deposition runs, increasing the applied power (i.e., to increase the sputter yield) increases the resulting film thickness. A linear dependence of the film thicknesses d_{B4C} on the generator power P was found and fitted by means of linear regression see Fig. 5

$$d_{B_4C}[\mathrm{nm}] = 25.76\frac{\mathrm{nm}}{\mathrm{kW}} \times P[\mathrm{kW}] - 1.50\,\mathrm{nm}$$

with a coefficient of determination $R^2 = 0.99956$. The offset in thickness is of about −1.50 nm for P = 0 W results from the uncertainty in the extraction of the thicknesses in the sample set using the fitting procedure for reflectivity.

A linear relation between film thickness and power is expected since the sputter yield is often related linearly to the applied DC power in the sputtering process.[50] The validity of the linear relation here is demonstrated in Fig. 5. The roughness parameter is almost constant with the applied power. Only a slight increase of the roughness from 0.2 nm RMS to 0.25 nm RMS for the samples deposited at 1200 W to the samples deposited at 2100 W was observed. This change in roughness can also be attributed to a variation of roughness from one Al_2O_3-substrate to the next in the range given by the specifications of the supplier. Therefore, increasing the generator power within the reported range does not have a negative effect on the coating quality and thus opens the possibility to increase the sputter velocity, i.e., the coating through put.

The length of the 100 mm wide converter plates was increased from 100 mm up to 300 mm and finally to 1430 mm. Neutron converter plates with dimensions 0.3 mm × 100 mm × 1430 mm were coated routinely with 1.2 μm of $^{10}B_4C$ as demonstrated in Fig. 6.

The use of long Al-substrates is motivated by two facts: First, large detector elements without stitching technology can be fabricated for large detectors. Second, the coating of long converter elements is more efficient compared to single short converter elements, since every single short element

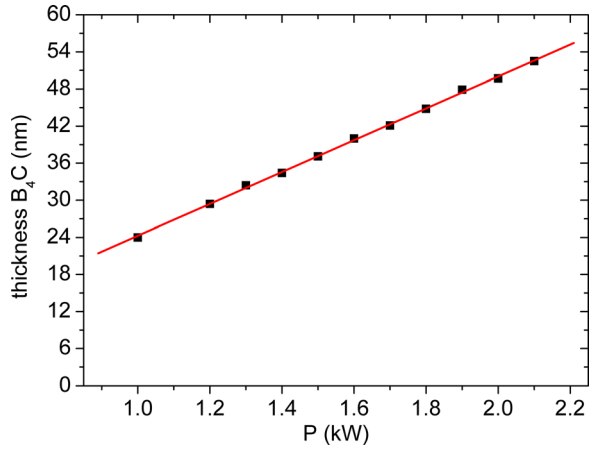

FIG. 5. Thicknesses of the $^{10}B_4C$ films as measurements present in Fig. 4 plotted vs. power on the sputter generator.

has to be fixed with two 10 mm wide clamps. These clamps cost space on the sample holder and reduce the effective deposition length. Finally, the long coated Al-converters can be cut to the desired length after the deposition, without delamination on the cutting edges (Figs. 7(c) and 7(d) (Multimedia view)). Moreover, choosing a thin substrate for the longest coatings provides a high mechanical flexibility of the conversion elements.

The high adhesion between the coating and the substrate (adhesive tape test as video is available online) makes it possible to bend the converter element without fracture or delamination of the 1.2 μm $^{10}B_4C$ coating as demonstrated in Fig. 7 (Multimedia view). This excellent mechanical property of the coated converters can be exploited for the development of neutron detectors with non-planar active area.

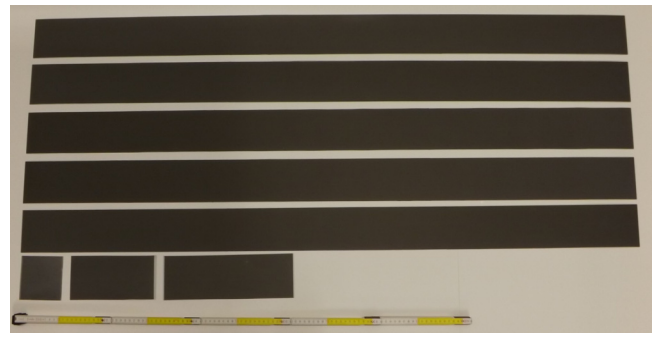

FIG. 6. Converter plates of various sizes coated with 1.2 μm $^{10}B_4C$. The largest coatings were fabricated on 100 mm × 1430 mm Al-plates. Folding rule below is 1 m long.

B. Depth profile investigations of boron carbide coatings

The atomic-scale structure of the B_4C layers was studied by means of XRD. Fig. 8 shows XRD measurements for B_4C films of 3 μm and 1 μm thickness sputter deposited on Al-substrates (Fig. 8). For comparison, the XRD-pattern of an uncoated Al-plate (100 mm × 100 mm) was recorded (black line in Fig. 8). Coatings sputter deposited onto Al and Si substrate at room temperature show no indication of crystalline boron carbide phases: for both layer thicknesses, the XRD patterns show only the texture reflections of the Al substrate (111), (200), (220), and (311) and an amorphous B_4C peak with a FWHM of about 10°. Therefore, crystalline long range order in this B_4C films can be excluded. Due to the larger scattering volume, the absolute intensity of the amorphous signal is stronger for the B_4C coating of 3 μm thickness. Using the Scherrer formula, the size of coherently scattering units perpendicular to the film surface can be estimated to be about 8–9 nm.

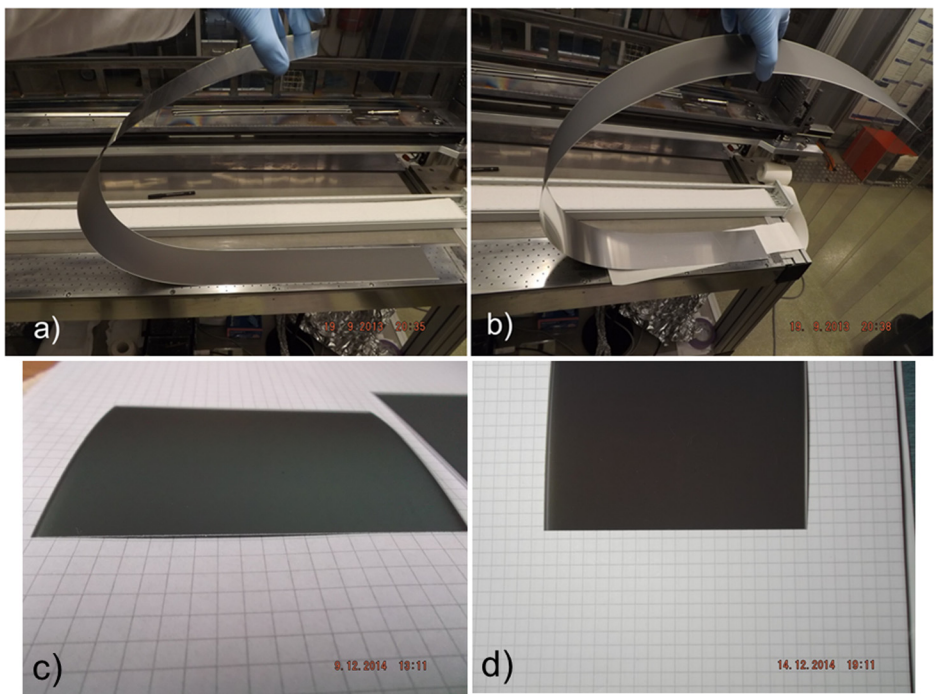

FIG. 7. Converter plate coated with 1.2 μm $^{10}B_4C$ with a size of 0.3 mm × 100 mm × 1430 mm bent inward (a) and outward (b). The photographs ((c) and (d)) demonstrate the cutting edge of a converter element when the cutting takes place after sputter deposition (photograph was taken 3 months after the cutting process). (Multimedia view) [URL: http://dx.doi.org/10.1063/1.4905716.1]

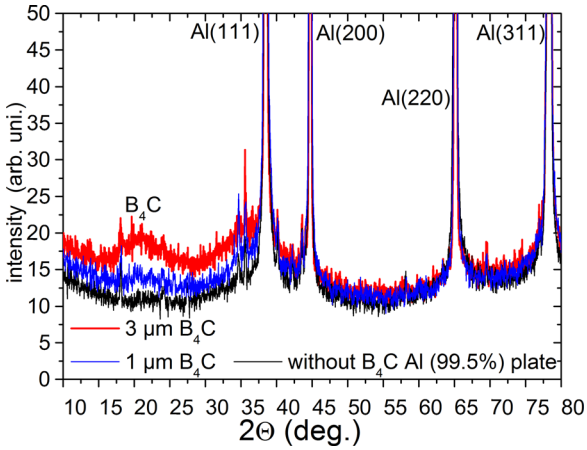

FIG. 8. XRD of B_4C layers of 3 μm and 1 μm thickness on Al (area: 100 mm × 100 mm). The black curve represents the XRD spectrum of the Al plate without B_4C coating.

Sputtering of B_4C at room temperature results in X-ray amorphous phase in agreement with Ref. 58.

SEM-micrographs of cross-sections through the B_4C coatings (see Fig. 9) exhibit no B_4C-crystallites on Ti/Si (100) in agreement with Ref. 58. Furthermore, the coatings are dense and adhere perfect to the underlying Si substrate by means of a Ti bonding layer. No cracks or voids are visible in the cross-section views. The thin film growth seems to be very uniform and dense with no hints of crystalline grains or boundaries. The reason for the observed type of growth is given below.

During the sputter deposition process, the strong covalent bonds of the deposited B_4C film reduce the mobility of adatoms[59,60] arriving at the film surface. As the coatings are deposited at room temperature, there is also no thermal mobilization of the adatoms. The inherent high quenching rate for the sputtering process, especially for substrates at room temperature, additionally reduces even further the mobility of adatoms. As a result, the formation of crystalline phase B_4C is prevented and an amorphous-phase is formed as expected.

A uniform conversion efficiency of neutrons into charged reaction products requires a structurally and compositionally uniform boron carbide coating in all three spatial directions of the converter. Therefore, also the levels and distributions of impurities (such as H and O, N) must be characterized. Particularly, the amount of heavy elements, which have an high stopping power and reduce the ion escape range for α and ^{7}Li, has to be monitored and has to be kept as low as possible. Furthermore, hydrogen has a high incoherent scattering cross section for cold and thermal neutrons. This scattering process causes a diffuse neutron background in the detector. Furthermore, in the sputter deposition process, the sputter yield is element specific. For targets consisting of two or more elements, the stoichiometry of the deposited film can thus differ from that of the target in the steady state of target-material erosion.[50] Therefore, it is important to compare the elemental composition of the deposited film with that of the target. Moreover, the mass density of the deposited material, i.e., the number density of ^{10}B atoms, can be varied in a certain range by changing the process conditions.[59,60] Consequently, a variation of mass density means a variation of conversion efficiency, which should be avoided.

XPS and SIMS were employed in combination with step-wise Ar ion etching to sample the chemical and isotopic depth profile of boron carbide coatings on Si substrates with natural oxide layer and Ti buffer layer and on Al substrates. All depth profiles are presented as functions of the etching time, which relates to the etched depth. Note that the etching yield is element specific. The etching time is therefore not a direct measure of the etched depth in the entire sample, i.e., interface widths for different substrate materials cannot be compared directly. SIMS can distinguish between the chemically identical but in mass (and neutron capture properties) different isotopes ^{10}B and ^{11}B and resolve their respective number density in the depth of the coating. The destructivity of both measurements methods results from the subsequent application of the etching step prior to the analysis process. Fig. 10 shows an XPS depth profile (left) based on element-separated peak analysis and a SIMS spectrum (right).

The XPS data were obtained from a B_4C layer of 440 nm thickness (etching time 800 to 6800 s). In this coating, the relative frequentness of boron is 78.6% and for carbon is 21.3%. The surface region (etching time 0 to 800 s) shows a slightly different composition of B and C and is addressed to the surface roughness of the film (similar also in Fig. 11). For the calculation of the relative frequentness for carbon and boron in the two component compound boron carbide, we use the following formula:[61] $rF_i = \frac{P_i}{P_C + P_B}$; $i = B, C$ with rF_i = relative frequentness of the component i in the boron carbide compound, P_i percentage of component i.

The percentage of the component i has been read off from the left plot of Fig. 10 as a horizontal line guided to the

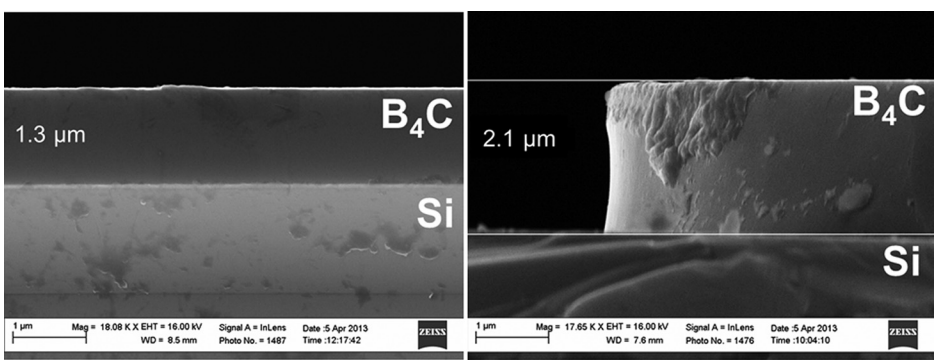

FIG. 9. SEM-micrographs of cross-sections of B_4C coatings of 1.3 μm and 2.1 μm thickness on Si (100) with a Ti bonding layer.

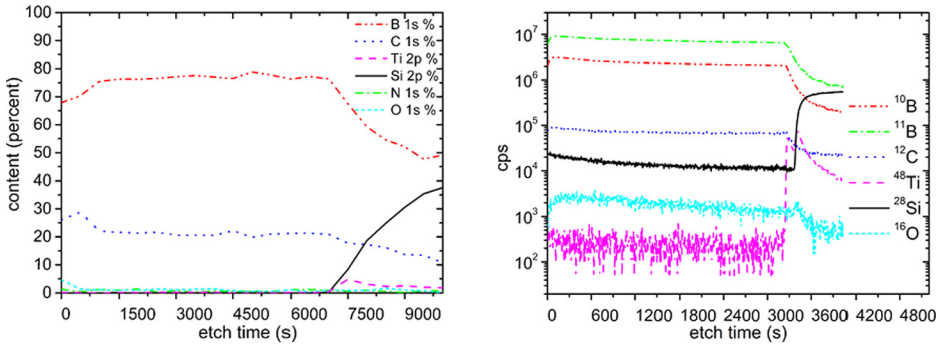

FIG. 10. XPS (left) and SIMS (right) depth profiles of $^{nat.}B_4C$ coatings of 440 nm and 490 nm thickness, respectively, sputter deposited on Ti/Si substrates.

eye in the depth range of the B_4C coating. The stoichiometric ratio between the amount of boron and carbon atoms is B/C = 3.7. The content of O and N is below 4 at. %. The SIMS data were recorded from a very similar sample of 490 nm thickness, using an approximately two times higher etching rate. In the SIMS spectrum, the relative signal height directly corresponds to the relative frequentness of an element or isotope. The SIMS spectrum in Fig. 10 (right panel) shows a relative frequentness of ^{11}B about 77.1% and for ^{10}B about 22.9% in the ensemble of boron atoms following the formula from Ref. 61 as above. Therefore, boron isotope ratio in this coating is $^{11}B/^{10}B = 3.4$, which is close to the natural isotope ratio of $^{11}B/^{10}B = 4.02$ resulting from natural isotopic composition of boron (^{11}B(80.1%) + ^{10}B(19.9%)).[13,62] The coating on Al substrate contains boron and carbon in a ratio of B/C = 3.6. The same levels of O and N content as in the coating on Si (Fig. 11) were detected. The B/C ratio is constant, i.e., the distribution of B and C is uniform throughout the coating depth.

By SIMS (see Fig. 12 left), the relative contents of ^{10}B and ^{11}B in an isotopically enriched $^{10}B_4C$ coating on Ti(50 nm)/Si was determined to be 93.6% and 6.4%, respectively. The enrichment of the ^{10}B isotope in the $^{10}B_4C$ coating is in very good agreement with the isotopic content of ^{10}B in the target material (mentioned in the experimental part: 95%, according to the supplier). Furthermore, the isotopic composition is constant over the entire thickness of the coating.

NRA employing the ^{10}B(α,p)^{13}C reaction is a non-destructive way of determining the concentration of the ^{10}B isotope in the entire $^{10}B_4C$ coating depth (1–2 μm penetration depth of 2 MeV α-particles). Fig. 12 (right) shows two proton emission energy spectra of a $^{10}B_4C$ coating of 1 μm thickness (black) and a $^{nat.}B_4C$ coating of 1.64 μm thickness (red), after bombardment with an α-particle beam of an energy of 2.0 MeV. The well-isolated peak between 1825 and 2140 keV emission energy corresponds to the ground state transition of the ^{10}B(α,p)^{13}C nuclear reaction. The contents of ^{10}B in the coatings are calculated from the integral areas below the corresponding peaks, weighted with the respective film thicknesses. The boron fraction of the $^{10}B_4C$ layer contains 90.5 ± 2.7 at. % of ^{10}B. Within the accuracy of the isotopic composition analysis via NRA, this value is in very good agreement with the result obtained by SIMS and data from the target supplier. Further by verifying the isotopic content of coatings by two independent methods (SIMS and NRA), the control of this parameter becomes in our case much more reliable. The access to SIMS (laboratory set-up) is easier than to an accelerator driven method like NRA. However, NRA allows determining the absolute number density of ^{10}B atoms in the coatings, thus providing a reference for the relative values obtained by SIMS.

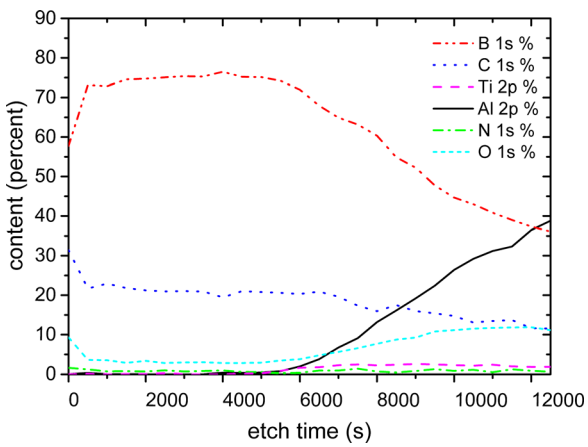

FIG. 11. XPS depth profile of a 440 nm $^{nat.}B_4C$ coating on Al.

As demonstrated above, NRA was used to determine the degree of enrichment of the ^{10}B isotope in the converter coating. Additionally, adapted NRA methods allow the measurement of the level and spatial distribution for hydrogen impurities as well as impurities of high Z elements. High Z impurities can be incorporated into the films when the sputtering process takes place at elevated power densities by sputtering off material from the walls of the deposition chamber or from constructional parts of the magnetron sources. Hydrogen is inherently present in the residual gas of the vacuum system and can also be incorporated during the deposition into the film. The disposition of these elements is of high relevance for the performance of converter coatings in the detector: Hydrogen causes an incoherent neutron scattering contribution and in this way the background level in the detector becomes enhanced. High-Z atoms stop the charged conversion reaction products on their escape way out of the converter layer much more effectively than lighter elements. Therefore, further chemical depth profiling was performed by NRA analyses of two $^{nat.}B_4C$ coatings of 1.17 μm thickness, deposited on Ti/Si substrates at generator powers of 800 W and 1900 W, respectively. These were carried out in a standard routine with a 2 MeV $^{2+}$He-ion beam provided by the tandem accelerator (RUBion) of the Ruhr-Universität Bochum, Germany. The ion

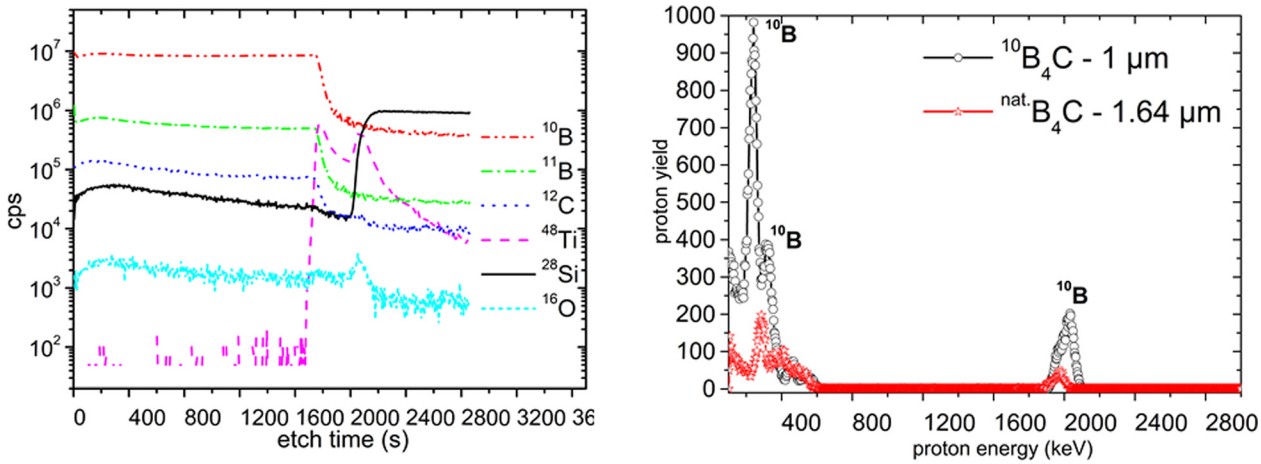

FIG. 12. Left: SIMS depth profile of a $^{10}B_4C$ coating of 100 nm thickness. Right: $^{10}B(\alpha,p)^{13}C$ proton yield spectra of a $^{10}B_4C$ coating of 1 μm thickness (black symbols) and a $^{nat.}B_4C$ coating of 1.64 μm thickness (red symbols) sputter deposited on Ti/Si.

incident angles were 0° and 55° with respect to the sample surface normal. Fig. 13 shows the RBS spectrum of the $^{nat.}B_4C$ coating sputtered at 800 W, measured under normal incidence of the He^{2+}-ion beam, with a fit (red curve) to the experimental data. Characteristic features of the spectrum are identified with the presence of the indicated elements and isotopes: The spectroscopic edge for the B_4C surface starts at an energy of 250 keV. A strong peak from the thin Ti layer appears around an energy of 500 keV. The surface edges of the ^{11}B and ^{12}C isotopes are expected to be at energies of 470 keV and 535 keV, respectively, and are thus covered by the Ti peak. Since the RBS scattering cross-section is proportional to Z^2, this method is highly sensitive to atoms with high atomic mass number. Further, the atomic mass number of Ti is high compared to those of Si, B, or C. Therefore, the small amount of Ti in the sample produces a comparatively high peak of backscattered α-particles. A Ti layer thickness of 46 ± 3 nm can be inferred from the width and height of the Ti peak, which is in good agreement with the Ti thickness expected for the given sputtering rate. The thickness of the B_4C layer can be deduced to amount to 1.17 μm from the position of the Ti peak (shifted towards lower energies by energy loss of the He^{2+} ions in the B_4C layer), assuming the B_4C layer to have almost bulk density. The small step at 380 keV is caused by the ^{10}B content of the natural boron. Up to an energy of 1350 keV, α-particles are backscattered from the uniformly distributed Ar-atoms in the coating depth. An amount of 1% to 1.5 at. % of Ar was extracted from the fitting of the RBS-data. This is a typical concentration of Ar in coatings produced by sputter deposition using Ar as process gas.

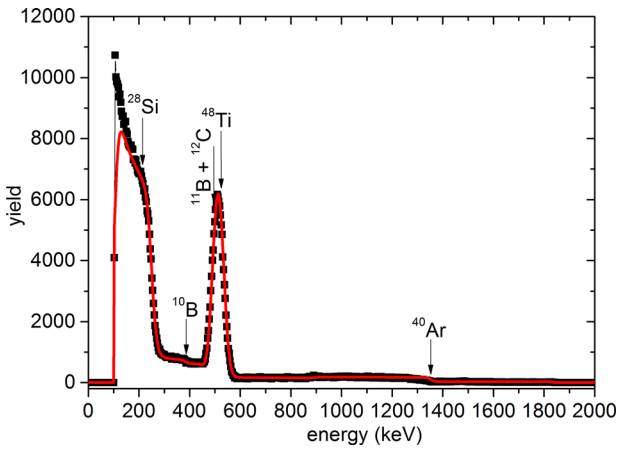

FIG. 13. RBS spectrum for a B_4C coating of 1.17 μm thickness on Ti/Si measured at an He^{2+}-ion beam at normal incidence. The fit to the data is indicated by the red curve. The generator power for the sputtering process of B_4C was 800 W. Thickness of the Ti buffer layer is 46 nm.

The red curve in the spectrum represents a simulation with the RBX-software using the layer parameters as described above. Using a scattering geometry with 55° incidence angle of the He^{2+} ions, the RBS-edges of ^{12}C, ^{11}B, and ^{10}B can be resolved better for a quantitative determination of their relative amounts. In non-normal incidence, the travel path of the He^{2+}-ions within the B_4C layer, and thus the scattering probability of the He^{2+}-ion on ^{10}B, ^{11}B, and ^{12}C, is increased (same principle as for increasing the neutron efficiency of a converter layer). Consequently, the Ti layer as well as the Si substrate is shifted out of the detection range of the incident He-ions and only the signals from C and B remain visible.

The resulting RBS spectrum is presented in Fig. 14. Indeed, the Si edge and the Ti peak disappeared from the spectrum and the ^{10}B, ^{11}B, and ^{12}C edges appear clearly. The red line in the spectrum of Fig. 14 is a RBX simulation, which describes the data very well with a natural isotopic composition of boron and a boron to carbon ratio of $B/C = 4 \pm 0.2$. The fit parameters match well with a detection of ^{10}B, ^{11}B, and ^{12}C edges (inset) at energies of 410, 470, and 535 keV. As seen in the spectrum for normal He^{2+} incidence (Fig. 13), an Ar edge is present at an energy of 1353 keV. The concentration of Ar-atoms was determined to a level of 1.5 at. % through the entire depth of the boron carbide converter coating. A multiple peak structure can be recognized in the energy range between 660 and 1070 keV, indicating thin layers of adsorbates—nitrides or oxides—of about a few monolayers thickness. For an inclined incidence of the He^{2+} ion beam on the sample, the RBS method is more sensitive to the constituents of the coating as well as to the impurities.

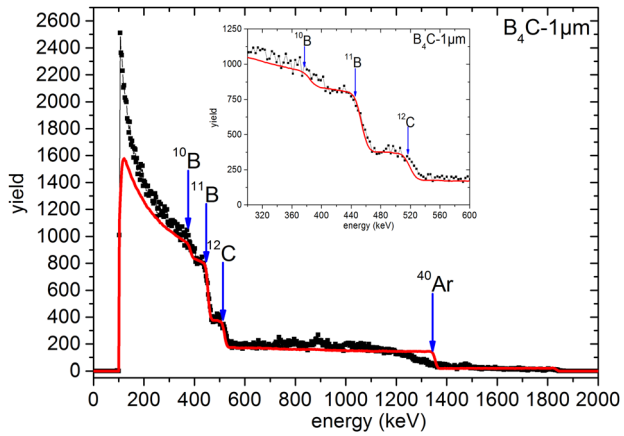

FIG. 14. RBS spectrum for a $^{nat.}B_4C$ coating on Ti/Si (same sample as in Fig. 13, the power for the sputtering process of B_4C was 800 W) measured at a He^{2+}-ion incident angle of 55° with respect to the sample surface normal. The fit to the data is indicated by the red curve. B_4C thickness: 1.17 μm, Ti thickness: 46 nm.

These adsorbates are typically found on top of thin films handled at ambient conditions, and have no effect on the neutron conversion performance of the converter coating.

RBS spectra can also provide information to quantify the degree of enrichment of the $^{10}B_4C$ coatings with respect to the amount of the ^{10}B isotope. The spectrum in Fig. 15 was measured for an isotopically enriched $^{10}B_4C$ coating deposited at a generator power of 1900 W. The incidence angle of He^{2+} ions was 55° with respect to the sample surface normal. The inverted heights of the ^{10}B and ^{11}B edges at energies of 410 and 470 keV correspond to the higher ^{10}B content of this $^{10}B_4C$ coating as compared to a $^{nat.}B_4C$ coating. The multiple peak structure between energy 660 and 1070 keV and the Ar-edge are more pronounced in the spectrum of the $^{10}B_4C$ coating. Additionally, small peaks at energies of 1450 and 1570 keV appear. These small peaks result from a very small concentration of V and/or Cr and Cu of about 0.1 at. %. These small contents are seen so clearly due to the high sensitivity of the RBS-method to high Z elements.[22,63] These impurities are often found in samples prepared at elevated sputtering power.

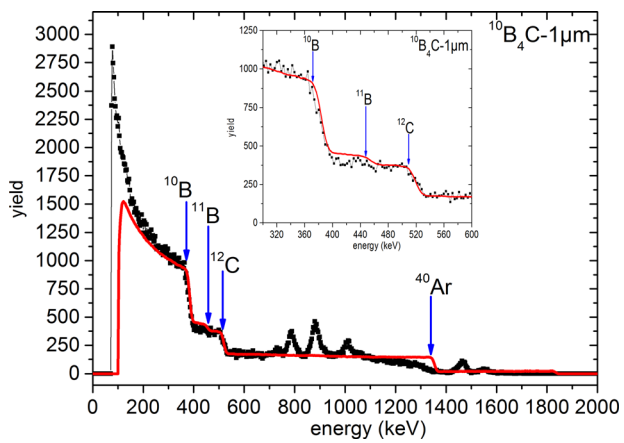

FIG. 15. RBS spectrum for a $^{10}B_4C$ coating on Ti/Si (The power for the sputtering process was 1900 W.) measured at a He^{2+}-ion incident angle of 55° with respect to the sample surface normal. The fit to the data is indicated by the red curve. $^{10}B_4C$ thickness: 1.17 μm, Ti thickness: 46 nm.

The higher sputtering power releases slightly more heavy atoms from constructive components of the UHV system to be incorporated in the converter coating.[64]

Finally, the investigations of the chemical composition of the coatings were completed with a depth profiling of the H content. The H concentration was determined by means NRA of the $H(^{15}N,\alpha\gamma)^{12}C$ reaction with the resonance at 6.4 MeV. In this experiment, the $^{10}B_4C$ coating of 1 μm thickness was irradiated with ^{15}N ions at varying energies, resulting in hydrogen detection at different depths of the converter layer (see Fig. 16). By plotting the number of events of coincident α-particles and γ-quant emissions as function of the ^{15}N beam energy, a hydrogen depth profile results as presented in Fig. 16. The energy axis can be transferred into a sample depth axis by calculating the stopping power of the ^{15}N beam (2.2 MeV/μm) in boron carbide.[65] The NRA spectrum in Fig. 16 exhibits only one local accumulation of H at 6.3 MeV (so-called surface peak). This accumulation corresponds to adsorbates of hydrogen containing molecules on the surface of the coating. A signal of hydrogen within the $^{10}B_4C$ coating is expected in the higher energy range from 6.4 MeV to 8.5 MeV (energies higher than the surface peak). In this energy range, a maximum signal level corresponding to 0.3 at. % of hydrogen is observed. Thus, the hydrogen impurity level in the $^{10}B_4C$ coatings is lower than 0.3 at. %. This result is highly relevant regarding the neutron detection process. The low amount of H impurities ensures a very low level of diffuse scattering of neutrons by hydrogen in the converter layer. Therefore, the converter coatings have a high potential for application in very low background neutron detectors.

In summary, sputter deposited, highly adhesive $^{10}B_4C$ coatings of 1.2 μm thickness have been prepared with a thickness uniformity in the range of 4%. The stoichiometry and isotopic composition of the sputter targets was transferred uniformly to the coating. The $^{10}B_4C$ coatings have a degree of enrichment on ^{10}B in the boron fraction of about 90–93 at. %. The hydrogen content in the B_4C coatings is below 0.3 at. %. These specifics prove an excellent suitability of the $^{10}B_4C$ coatings for neutron detection applications. First, neutron conversion test measurements are presented below.

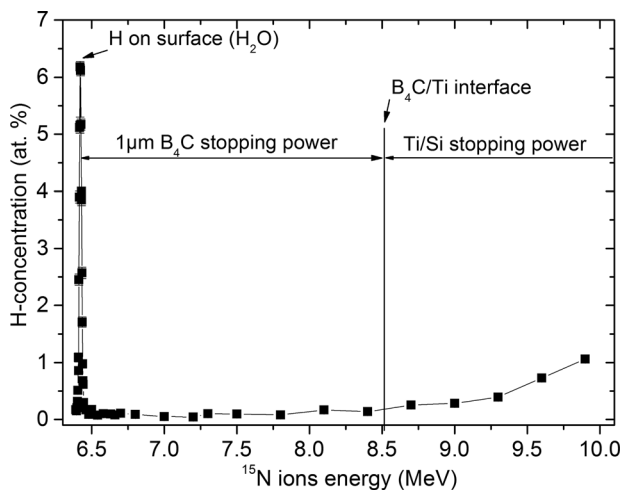

FIG. 16. Hydrogen profile in a $^{10}B_4C$ coating of 1 μm thickness measured by the $H(^{15}N, \alpha\gamma)^{12}C$ reaction.

C. Neutron quantum efficiency of $^{10}B_4C$ coatings

The relative quantum efficiency of $^{10}B_4C$ coatings was evaluated by measurements at the ToF-reflectometer REFSANS.[54,55] For the test detector, an Al window of 6 mm thickness was chosen. At this thickness, the window can withstand many cycles of pressure changes during the opening and closing the detector housing for exchanging the converter samples. In the final detector design, the thickness of the Al window would be reduced to 1 to 2 mm to minimize neutron absorption by Al. For the measurements presented here, the detector was equipped with four amorphous $^{10}B_4C$ converter coatings of 1 μm thickness. The converter plates were positioned in the same horizontal plane. The test detector was mounted at the sample position on the REFSANS goniometer so that the collimated incident beam hits the converter plates in the test detector at a grazing incidence angle. A detailed discussion of the inclined geometry detector concept and its performance will be the issue of a following publication on detector engineering and design. Width and height of the incident beam as well as the detector position in the beam were chosen so as to ensure that the beam footprint on a converter plate was always significantly smaller than the converter plate itself, and that the footprint was always placed far away from the edges of the converter element. The measurement geometry corresponds to the geometry depicted in the concept sketch in Fig. 17 ($\Theta = \Theta_{in}$). The incident angle of the primary beam with respect to the converter layer surface was varied in the range of $\Theta_{in} = 1^\circ - 4^\circ$.

To cover the cold neutron energy range, two ToF-spectra of incident neutrons were chosen by specific chopper settings, which selected neutron wavelength ranges $\lambda_{s1} = 2$–10 Å and $\lambda_{s2} = 8$–30 Å. These spectra were read out by integration of event pulses over every individual wire of the cathode system, separately for both x- and y-directions of the active area of the 2D detector. The spectra measured by the test detector were normalized to a spectrum measured by a monitor, a single wire tube detector operating in ToF-mode, at the same position. At this measurement position, the horizontal width of the primary beam was about 20 mm (given by the divergence of the instrument), and its height was about 0.6 mm (about 0.3 mm directly after the collimation system at a distance of 500 mm from the measurement position).

The monitor tube was oriented horizontally with the tube axis perpendicular to the primary beam direction. Additionally, the monitor tube had an inner diameter of 25.4 mm, an active tube length of 200 mm, and was filled with 10 bars of ^{3}He. This monitor reliably determined the primary incident neutron flux, capturing almost 99.9% of the incoming cold neutrons because of its high ^{3}He atom density. The relative spectral quantum efficiency of the test detector (i.e., the number of neutron events measured by the test detector divided by the number of neutron events measured by the ^{3}He monitor) is plotted for three incidence angles in Fig. 18. The peak to peak scattering of the data points in the efficiency curves in Fig. 18 is about 7% at maximum. The relative large scattering in all experimental curves as well as the increased data scattering with λ is related to a small wave length binning of 0.007 Å in the available data evaluation. A small available numbers of neutrons in the respective wavelength slots from the cold source increase further the scattering of these data point. Therefore, the following discussion refers to the lower limit of the achieved efficiency.

For an incidence angle of $\Theta_{in} = 1^\circ$, the relative quantum efficiency of the test detector ranges from approximately 65% to 92% for neutrons of $\lambda \geq 5$ Å. The local minima in efficiency at about 4.05 Å and 4.8 Å are attributed to Bragg scattering at the Al entrance window.[66] This entrance window is not present in the measurements with the ^{3}He-monitor used for normalization since the monitor tube is made of stainless steel only. Additionally, an overall attenuation of

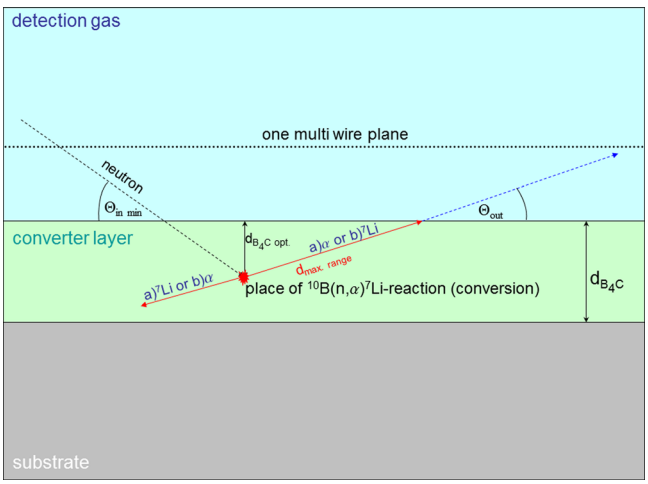

FIG. 17. Trajectories of a neutron and reaction products in a conversion reaction with a boron nucleus in a multi-wire chamber detector. The thickness of the converter layer is d_{B4C}. There are two possible configurations for the reaction products ^{7}Li and α to leave the point of conversion on back-to-back trajectories, as indicated by labels (a) and (b). d_{B4Copt} denotes the optimum converter layer thickness as given by the maximum ion range $d_{max\ range}$ of ^{7}Li, which still allow a ionization of the detection gas above the converter in the conversion reaction.

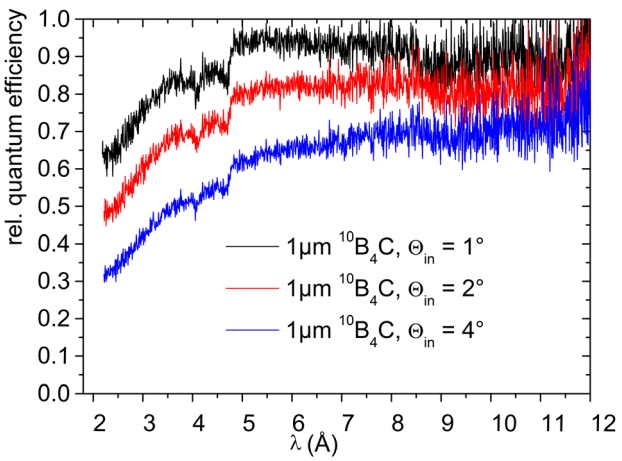

FIG. 18. Spectral quantum efficiency for an amorphous $^{10}B_4C$ coating of 1 μm thickness, measured in ToF mode at neutron incidence angles Θ_{in} of 1°, 2°, and 4°, respectively, and normalized to the spectral quantum efficiency of a 1 in. ^{3}He tube monitor. A quantum efficiency value of 1.0 means 100% of the quantum efficiency of a 1 in. counter tube filled with 10 bars of ^{3}He. The wave length binning is 0.007 Å.

the neutron flux is expected due to energy-dependent absorption in the Al window. An attenuation of the neutron flux of about 2.5% at $\lambda = 1.8$ Å was estimated from the absorption cross-section and the thickness of the Al window as shown in Fig. 19.

The curve progression of the measured relative quantum efficiency as function of the incident angle Θ_{in} in Fig. 18 can be compared to the calculated progression of the neutron absorption for conditions as given in the experiment. The maximum length of the absorption path is given by $l_{max} = \frac{d_{B4C}}{\sin(\Theta_{in})}$. Fig. 19 presents the calculated absorption as a function of the neutron wavelength for incidence angles of 1°, 2°, and 4°. The calculation assumed a mass density of $^{10}B_4C$ of ρ=2.51 g/cm^3 and the attenuation length as a function of neutron energy was determined using data from Ref. 67. Further, in Fig. 19 (green curve) the transmission of the 6 mm thick detector window has been calculated as function of the neutron wavelength. The absorption curves for 1°, 2°, and 4° have been multiplied by the transmission curve of the 6 mm Al window. Exemplary for the incidence angles 1°, 2°, and 4°, the absorption factors are listed here for neutrons with a wavelength of 1.8 Å:

(a) $\Theta_{in} = 1°$: $l_{max} = 53.7$ μm; $\varepsilon_{abs} = 92.3\%$.
(b) $\Theta_{in} = 2°$: $l_{max} = 28.6$ μm; $\varepsilon_{abs} = 72.4\%$.
(c) $\Theta_{in} = 4°$: $l_{max} = 14.3$ μm; $\varepsilon_{abs} = 47.3\%$.

The comparison of the calculated absorption and measured efficiency curves yields up to 30% reduced efficiency compared to the absorption factors for short wavelengths neutrons (2–4 Å) (also indicated by the exemplarily calculated absorption factors above). This discrepancy will be elucidated by a detailed discussion of the detection concept in a forthcoming publication following calculations presented in Refs. 68 and 69. For neutrons of the wavelength spectrum from 5 to 12 Å, the absorption (Fig. 19) and efficiency curves (Fig. 18) converge to the transmission curve of the Al detector window, which has a negative slope as a function of wavelength. This influence of the Al window as used in the test detector in terms of limited transmission and a resulting reduction of the efficiency can be recognized most distinctly in the slight negative slope of the efficiency curve for the incident angle of 1° shown in Fig. 18. The curves for 2° and 4° in the same figure do not reach the saturated state of efficiency. Comparing Figs. 18 and 19, the same relative increase of quantum efficiency and of absorption with decreasing angle of incidence (i.e., increasing neutron path length) is observed. Since absorption and quantum efficiency are directly related to each other, further effects like channeling, etc., can therefore be excluded for the experimental data in Fig. 18.

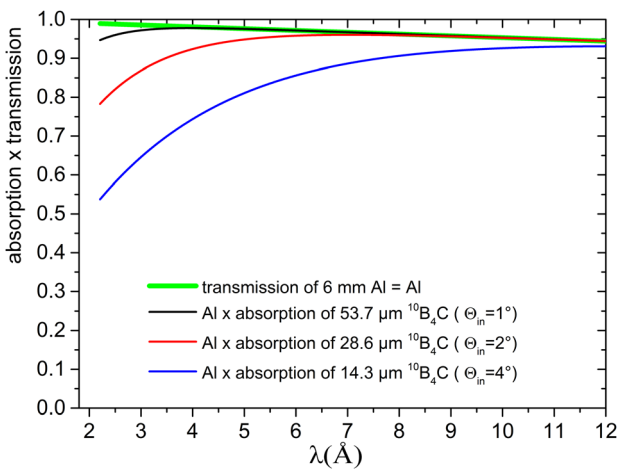

FIG. 19. Calculated absorption curves as a function of the neutron wavelength for a $^{10}B_4C$ coating of 1 μm thickness and neutron incidence angles Θ_{in} of 1°, 2°, and 4°, respectively. The absorption curves have been multiplied by the transmission curve for the 6 mm Al detector window in green. The value of 1.0 means 100%.

IV. CONCLUSION

Natural and ^{10}B enriched large-area boron carbide coatings were prepared by means of magnetron sputtering. Using the complementary probes, x-rays, neutrons, and ions these, boron carbide coatings have been comprehensively investigated and their excellent quality was demonstrated. The film properties were characterized with respect to layer thickness, film adhesion, phase formation, thin film growth, chemical composition, impurity, and isotopic content. A coating thickness of up to 2 μm was achieved for amorphous and highly adhesive B_4C and $^{10}B_4C$ coatings. Over the entire deposited length and width of these coatings, their thickness deviates by about 4% compared to the total thickness. The coatings deposited on Si substrates and on Al plates show uniform elemental and isotopic composition and homogeneous distribution of the constituents throughout their entire depth. The detected levels of impurities of O (below at. 5%), N (below at. 2%), and H (below at. 0.3%) are very low. About 2.5 m^2 of these highly uniform $^{10}B_4C$ and natural B_4C coatings with a thickness of 1.2 μm were deposited with excellent mechanical properties for detector prototypes. Routinely, a coating of about 1.43 m long Al plates is possible in one step, which is an advantage for future detector development. Experimental determinations of neutron detection efficiency were conducted for the range of thermal and cold neutrons at an incident angle of 1° to 4° of the neutron beam with respect to the converter coating surface. Relative quantum efficiencies from 65% to 90%, normalized to a 1 in. monitor wire tube filled with 10 bars of ^3He were measured. Thus, the advanced $^{10}B_4C$ coatings are promising candidates for replacing ^3He in large scale neutron detectors. Transferring the presented preparation process to a large-scale industrial system would deliver highly uniform $^{10}B_4C$ neutron converter coatings for alternative, ^3He-free large-area neutron detection systems.

ACKNOWLEDGMENTS

This work was carried out as the German in-kind contribution to the ESS preconstruction and the ESS design update phase founded by the BMBF (BMBF-Project 05E11CG1: "Verbundprojekt: Mitwirkung der Zentren der Helmholtz-Gemeinschaft und der Technischen Universität München an der Design-Update-Phase der ESS") to develop crucial components for the European Spallation Source (ESS) in cooperation with the industrial partner DENEX GmbH. We thank T. Kühl and E. Prätzel (DENEX GmbH) for their craftsmanship in the fabrication of the test detector.

We thank the RUBION Team at the Ruhr-Universität Bochum for a comprehensive support in nuclear material analysis. G.N. thanks the REFSANS beam line team for their very comprehensive support during all the beam times. Finally, we thank Dr. Botters in the Filmetrics GmbH for the introduction and the opportunity to perform the spectral reflectance measurements.

[1]See http://nmi3.eu/neutron-research/grand-challenges/health-and-life-sciences.html for "Health and Life sciences" for the wide range of neutron scattering methods requested in health and life science.
[2]G. A. Webster and A. N. Ezeilo, Physica B **234–236**, 949–955 (1997).
[3]D. Kramer, Phys. Today **64**(5), 20 (2011).
[4]See http://eval.esss.lu.se/cgi-bin/public/DocDB/ShowDocument?docid=274 for European Spallation Source—Technical Design Report, ESS-2013-001, 2013.
[5]W. L. Davidson, G. A. Morton, C. G. Shull, and E. O. Wollan, *Neutron Diffraction Analysis of NaH and NaD* (U.S. Department of Energy, 1947).
[6]C. G. Shull and E. O. Wollan, *The Diffraction of Neutrons by Crystalline Powders* (Oak Ridge National Laboratory, U.S. Department of Energy, 1947).
[7]G. F. Knoll, *Radiation Detection and Measurement*, 4th ed. (John Wiley & Sons, 2010), p. 534.
[8]C. M. Lederer and V. S. Shirley, *Table of Isotopes* (John Wiley & Sons, 1978).
[9]L. T. Aldrich and A. O. Nier, Phys. Rev. **74**, 1590–1594 (1948).
[10]D. A. Shea and D. Morgan, Report No. R41419, 2010.
[11]S. Son and N. J. Fisch, Phys. Lett. A **329**(1–2), 76–82 (2004).
[12]J. Santarius, "Talk: "Lunar ^{3}He and Fusion Power"," in IEEE Rock River Valley Section, Rockford, Illinois, 28 September 2004.
[13]H. H. Binder, *Lexikon der chemischen Elemente* (S. Hirzel Verlag, Stuttgart, 1999).
[14]Mineral Commodity Summaries: Boron, United States Geological Survey, 2008, Retrieved 2008-09-20.
[15]M. O. Klein, Ph.D. thesis, Ruprecht Karls Universität, Heidelberg, 2000.
[16]T. L. van Vuure, J. F. Ankner, J. F. Browning, L. G. Clonts, M. L. Crow, R. G. Cooper, I. Remec, J. D. Richards, R. A. Riedel, and J. L. Robertson, IEEE Trans. Nucl. Sci. **57**(1), 323 (2010).
[17]R. Arnaldi, E. Chiavassa, A. Colla, P. Cortese, G. Dellacasa, N. De Marco, A. Ferretti, M. Gallio, A. Musso, C. Oppedisano, A. Piccotti, F. Poggio, E. Scalas, E. Scomparin, F. Sigaudo, and E. Vercellin, Nucl. Instrum. Methods Phys. Res., Sect. B **213**, 284–288 (2004).
[18]C. Höglund, J. Birch, K. Andersen, T. Bigault, J.-C. Buffet, J. Correa, P. van Esch, B. Guerard, R. Hall-Wilton, J. Jensen, A. Khaplanov, F. Piscitelli, C. Vettier, W. Vollenberg, and L. Hultman, J. Appl. Phys. **111**, 104908 (2012).
[19]V. F. Sears, "Neutron scattering lengths and cross section," Neutron News **3**(3), 26 (1992).
[20]See http://atom.kaeri.re.kr for Cross Section Plotter des Korea Atomic Energy Research Institute.
[21]Y. Saito, K. Mishima, T. Hibiki, A. Yamamoto, J. Sugimoto, and K. Moriyama, Nucl. Instrum. Methods Phys. Res., Sect. A **424**, 142 (1999).
[22]E. Rutherford, "The scattering of α and β particles by matter and the structure of the atom," Philos. Mag. Ser. 6 **21**, 669–688 (1911).
[23]H. Geiger and E. Marsden, "On a diffuse reflection of the α-particles," Proc. R. Soc. **82**, 495–500 (1909).
[24]J. P. Biersack and L. Haggmark, Nucl. Instrum. Methods **174**, 257 (1980).
[25]J. F. Ziegler, J. P. Biersack, and U. Littmark, *The Stopping and Range of Ions in Solids* (Pergamon, New York, 1985), Vol. 1.
[26]M. Henske, M. Klein, M, Köhli, P. Lennert, G. Modzel, C. J. Schmidt, and U. Schmidt, Nucl. Instrum. Methods Phys. Res., Sect. A **686**, 151–155 (2012).
[27]K. Andersen, T. Bigault, J. Birch, J. C. Buffet, J. Correa, R. Hall-Wilton, L. Hultman, C. Höglund, B. Guérard, J. Jensen, A. Khaplanov, O. Kirstein, F. Piscitelli, P. Van Esch, and C. Vettier, Nucl. Instrum. Methods Phys. Res., Sect. A **720**, 116–121 (2013).
[28]J. Correa, Ph.D. thesis, University of Zaragoza, Zaragoza, 2012.
[29]I. Stefanescu, Y. Abdullahia, J. Birch, I. Defendi, R. Hall-Wilton, C. Höglund, L. Hultman, D. Seiler, and K. Zeitelhack, Nucl. Instrum. Methods Phys. Res., Sect. A **727**, 109–125 (2013).
[30]R. R. Rigdway, Am. Electrochem. Soc. **66**, 117 (1934).
[31]A. Lipp, 14-28-33, 7, 47, Techn. Rundschau, 1966.
[32]F. Thevenot, Key Eng. Mater. **56–57**, 59–88 (1991).
[33]C. L. Chiang, H. Holleck, and O. Meyer, Nucl. Instrum. Methods Phys. Res., Sect. B **91**, 692–695 (1994).
[34]F. Laves, Zachr. Ges. Wiss. Göttingen, Mathem-Physik Kl. Neue Folge **1**, 57–58 (1934).
[35]G. Will and K. H. Kossobutzki, "An XRD analysis of boron carbide, $B_{13}C_2$," J. Less-Common Met. **47**, 43–48 (1976).
[36]T. Fujii, Y. Mori, H. Hyodo, and K. Kimura, J. Phys.: Conf. Ser. **215**, 012011 (2010).
[37]M. A. McKernan, Surf. Coat. Technol. **49**, 411 (1991).
[38]A. Lousa, E. Martinez, J. Esteve, and E. Pascual, Thin Solid Films **355**, 210 (1999).
[39]M. U. Guruz, V. P. Dravid, and Y. W. Chung, Thin Solid Films **414**, 129 (2002).
[40]R. Soufli, S. L. Baker, J. C. Robinson, E. M. Gullikson, T. J. McCarville, M. J. Pivovaroff, P. Stefan, S. P. Hau-Riege, and R. Bionta, SPIE Proceedings **7361**, 73610U (2009).
[41]L. Vandenbulcke and G. Vuillard, J. Less-Common Met. **82**, 49 (1981).
[42]U. Jansson and J. O. Carlsson, Thin Solid Films **124**, 101–107 (1985).
[43]R. J. K. Wood, D. W. Wheeler, D. C. Lejeau, and B. G. Mellor, Wear **233–235**, 134–150 (1999).
[44]H. Pedersen, C. Höglund, J. Birch, J. Jensen, and A. Henry, Chem. Vap. Deposition **18**, 221–224 (2012).
[45]M. Störmer, A. Liard-Cloup, F. Felten, S. Jacobi, B. Steeg, J. Feldhaus, and R. Bormann, "Investigations of large x-ray optics for free electron lasers," Proc. SPIE **5533**, 58–65 (2004).
[46]M. Störmer, F. Siewert, and J. Gaudin, Proc. SPIE **8078**, 80780G (2011).
[47]M. Störmer, Ch. Horstmann, G. Nowak, R. Kampmann, J. Hedde, European patent application 14176907.5 - 1353 (14 July 2014).
[48]Bruker Analytical X-ray System, REFSIM-Instruction-Manual, Karlsruhe, 1996.
[49]H. G. Tompkins and W. A. McGahan, *Spectroscopic Ellipsometry and Reflectometry: A User Guide* (John Wiley & Sons, 1999), p. 113.
[50]M. Ohring, *Material Science of Thin Films (Deposition and Structure)*, 2nd ed. (Academic Press, 2002).
[51]RBX developed by E. Kótai, Research Institute for Particle and Nuclear Physics, Hungary, 1985.
[52]H. Chen, X. M. Wang, L. Shao, J. R. Liu, A. C. Yen, and W.-k. Chu, Nucl. Instrum. Methods Phys. Res., Sect. B **211**, 1–6 (2003).
[53]W. A. Lanford and M. J. Rand, J. Appl. Phys. **49**, 2473 (1978).
[54]R. Kampmann, V. Deriglazov, M. Haese-Seiller, M. Marmotti, M. Tristl, and E. Sackmann, Physica B **276–278**, 212–213 (2000).
[55]R. Kampmann, M. Haese-Seiller, V. Kudryashov, B. Nickel, C. Daniel, W. Fenzl, A. Schreyer, E. Sackmann, and J. Rädler, Physica B **385–386**, 1161–1163 (2006).
[56]Online Instrumental Report FRM-II, 2012.
[57]H. Kiessig, "Interferenz von Röntgenstrahlen an dünnen Schichten," Ann. Phys. **402**, 769–787 (1931).
[58]D. M. Makowiecki, A. F. Jankowski, M. A. McKernan, and R. J. Foreman, J. Vac. Sci. Technol., A **8**(6), 3910 (1990).
[59]J. A. Thornton, Ann. Rev. Mater. Sci. **7**, 239–260 (1977).
[60]J. J. Cuomo, J. Doyle, J. Bruley, and J. C. Liu, Appl. Phys. Lett. **58**, 466 (1991).
[61]T. Bayes and R. Price, "A letter to J. Kanton "An essay towards solving a problem in the doctrine of chances"," Philos. Trans. R. Soc. London **53**, 370–418 (1763).
[62]P. Argust, Biol. Trace Element Res. **66**(1–3), 131–143 (1998).
[63]S. Rubin, T. O. Passell, and E. Bailey, "Chemical analysis of surfaces by nuclear methods," Anal. Chem. **29**, 736 (1957).
[64]P. Vuoristo, T. Mätylä, P. Kettunen, and R. Lappalainen, Thin Solid Films **204**, 297–311 (1991).
[65]See http://www.srim.org/ for SRIM.
[66]W. Kockelmann, G. Frei, E. H. Lehmann, P. Vontobel, and J. R. Santisteban, Nucl. Instrum. Methods Phys. Res., Sect. A **578**, 421–434 (2007).
[67]See www.ncnr.nist.gov/cgi-bin/neutcalc for this online calculator was used to get the attenuation lengths for neutrons ($\lambda = 1.8$ Å) in Al and $^{10}B_4C$.
[68]F. Piscitelli and P. Van Esch, JINST **8**, P04020 (2013).
[69]D. S. McGregor, M. D. Hammig, Y.-H. Yang, H. K. Gersch, and R. T. Klann, Nucl. Instrum. Methods Phys. Res., Sect. A **500**, 272–308 (2003).